One-pot synthesis of carbon-supported AuCo and AuNi nanoalloys for the oxygen reduction reaction in alkaline media

Francisco Acosta-Arreazola, Nora A Garcia-Gomez, Marian Chatenet, Vincent Martin, Israel López, Eduardo M Sánchez

One-pot synthesis of Carbon-supported AuCo and AuNi nanoalloys for the oxygen reduction reaction in alkaline media

Francisco Acosta-Arreazola[1,3], Nora A. Garcia-Gomez[1,3*], Marian Chatenet[2*], Vincent Martin[2], Israel López[3], Eduardo M. Sánchez[1]

[1]Universidad Autónoma de Nuevo León, UANL, Facultad de Ciencias Químicas, FCQ, LabMat2: Almacenamiento y Conversión de Energía, Av. Universidad S/N Ciudad Universitaria San Nicolás de los Garza Nuevo León, C.P. 66455 México.

[2]University Grenoble Alpes, University Savoie Mont Blanc, CNRS, Grenoble INP (Institute of Engineering and Management University Grenoble Alpes), LEPMI, 38000 Grenoble, France.

[3]Universidad Autónoma de Nuevo León, UANL, Facultad de Ciencias Químicas, FCQ, Centro de Investigación en Biotecnología y Nanotecnología, CIBYN, PIIT, Apodaca, Nuevo León, C.P. 66628 México.

*Corresponding authors: Nora A. Garcia-Gomez; noragarcian@uanl.edu.mx; Telephone number: +52(81)83294000. And Marian Chatenet; marian.chatenet@grenoble-inp.fr; Telephone number: +33 476 82 65 88.

Abstract

Carbon-supported bimetallic AuCo and AuNi electrocatalysts were prepared from one-pot wet-chemistry techniques (ethylene glycol-stabilization and aqueous-solution stirring) and evaluated for the oxygen reduction reaction (ORR) in alkaline media. All the materials consist of near-spherical nanoparticles that show varying sizes and extent of agglomeration. While the ethylene-glycol method produced less agglomerated particles, the stirring method produced smaller ones. X-Ray photoelectron (XPS) analyses demonstrated the change in the binding energies of Au $4f_{5/5}$ and Au $4f_{7/2}$ versus the expected values for pure gold, pointing at the formation of alloyed nanoparticles. The combination of such electronic effects and morphology led the AuNi/C-EG nanoalloy to a good compromise between materials cost (versus Au/C) and ORR activity: the onset potential and half-wave potential for the oxygen reduction reaction are 0.833 and 0.600 V *vs.* RHE, respectively, corresponding to a specific activity 10% greater than that for Au/C at 0.85 V *vs.* RHE. The carbon-supported AuNi nanoalloy possesses undoubtable potential to be used as an electrocatalyst for the electroreduction of oxygen in alkaline environments.

Keywords: Au-based nanoalloys; non-platinum materials; cathode electrocatalyst; oxygen reduction reaction.

1 Introduction

Fuel cells are electrochemical devices that convert the chemical energy of a fuel into electrical energy. When hydrogen is the fuel and oxygen (air) the oxidant, the only reaction products are water, heat, and electricity [1]. The oxygen reduction reaction (ORR) remains as one of the main bottlenecks in the performance of these devices [2]. At present, platinum and its alloys are the most widely used materials to catalyze the ORR [3-5]. Nevertheless, it has been demonstrated that Pt/C nanomaterials are very unstable in alkaline media, losing up to 60% of their ECSA after 150 only cycles between 0.1 and 1.23 V *vs.* RHE [6], that can mimic start-stop operation. Zhang and collaborators demonstrated that by adding Au clusters into Pt nanoparticles, the resulting electrocatalysts were stabilized, and their dissolution got prevented [7]. Also, Park and colleagues proved that Au alloying with Pt nanoparticles increased the ORR electrocatalytic activity [8].

Indeed, Au is more stable in alkaline media than Pt [9]; however, its electrocatalytic activity towards the ORR is lower due to the (too) week bonding of atomic oxygen on its surface, which indicates that the barrier for oxygen dissociation is large [10]. A widely-used strategy to develop Au-based electrocatalysts for the ORR is to alloy Au with 3d-transition metals [11-13]. Jiali and collaborators prepared AuNi dendrites by combining electrodeposition and electrochemical dealloying methods. They concluded that the presence of nickel into the gold lattice led to a positive shift in the d-band center (Fermi level), which favored the adsorption of oxygen species and enhanced the electrochemical activity towards the ORR [14]. To improve the distribution and composition of Au and Ni, Jiali and colleagues developed a one-pot method to prepare dealloyed AuNi nanodendrites. The as-synthetized material showed a half-wave potential 81 mV more positive, and a specific activity (at 0.85 V *vs.* RHE) 3.1 times higher than Pt/C [15]. The work published by Hongyu and collaborators is another example of the importance of electronic changes and nanoporous construction on the electrocatalytic activity of gold. They prepared AuCu aerogels with specific and mass activities 4.5 and 6.3 times higher than Pt/C for the ORR, respectively [16]. These strategies demonstrate that AuM nanostructures can outperform Pt for alkaline ORR. However, it is no secret that dendritic and aerogel-based nanostructures are not easy to implement in real fuel cell electrodes without substantial loss of apparent activity, as demonstrated for Pt-based PEMFC electrodes [17]. So, it is wise, also, to search for advanced carbon-supported Au-based electrocatalysts,

that could substitute Pt-based ones. $NaHB_4$ reduction in ethylene glycol at room temperature is a simple method to prepare highly dispersed precious and precious:transition metal particles on a carbon support. It has been demonstrated on several occasions as for example for PdNi/N-doped graphene [31] and Pt/MWNT for components of direct fuel cells [32]. The $NaBH_4$ reduction in the ethylene glycol method allows obtaining particles with sizes less than 5 nm, and the above is because the formed glycoxide acts as efficient stabilizers. A greener methodology for the preparation of such particles is to work in aqueous media since no solvents need to be added. As demonstrated by Berdan and collaborators, the co-reduction of Pd, Au, and Co can be carried out by adding $NaBH_4$ in deionized water [33]. Despite the above, to our knowledge, there are no publications about the synthesis of carbon-supported Au-based nanoalloys via the two previous methods and their application as electrocatalysts for the oxygen reduction reaction in alkaline electrolytes. In that frame, this work builds on these earlier works and aims to compare the electrocatalytic activity towards the ORR of carbon-supported AuNi and AuCo nanoalloys prepared via two methodologies: ethylene-glycol stabilization and stirring method in aqueous solution, the latter being compatible with an approach of green chemistry. These methodologies find their interest in the fact that ethylene-glycol was proven a suitable stabilizer agent, that prevents extensive nanoparticle agglomeration and enables to produce carbon-supported materials with a specific particle size distribution [18-20].

2 Materials and methods

Gold(III) chloride ($HAuCl_4$ 99%, Sigma-Aldrich, San Luis, MO, USA), cobalt(II) nitrate hexahydrate ($Co(NO_3)_2$-$6H_2O$ ACS reagent ≥98%, Sigma-Aldrich, San Luis, MO, USA), nickel(II) nitrate hexahydrate ($Ni(NO_3)_2$-$6H_2O$ 99.99%, Sigma-Aldrich, San Luis, MO, USA), ethylene glycol (ReagentPlus ≥99%, Sigma-Aldrich, San Luis, MO, USA), Carbon black (C_{black} acetylene, 99.9%, S. A. 80 $m^2\ g^{-1}$, Alfa Aesar, Ward Hill, MA, USA), ethanol (Absolute, CTR Scientific, Monterrey, N. L., Mexico), Nafion® 117 (5% p/p isopropanol, Sigma-Aldrich, San Luis, MO, USA), isopropanol (ACS 99.5%, Alfa Aesar, Ward Hill, MA, USA), and potassium hydroxide (KOH 99.98%, Alfa Aesar, Ward Hill, MA, USA) were used as-received without further treatment. Ultrapure Ar (99.999 %, Air Liquide, Paris, France) and O_2 (≥ 99.999%, Air Liquide, Paris, France)

were used to deaerate the electrolyte solution for experiments in supporting electrolyte, and saturate the electrolyte for oxygen reduction reaction experiments, respectively.

2.1 Preparation of carbon-supported Au:Co and Au:Ni nanoalloys by stirring method (Au:Co/C-S, Au:Ni/C-S)

Au:Co/C-S and Au:Ni/C-S catalysts were prepared by the so-called stirring method (S) at room temperature. To carry it out, proper volumes of 0.001 M $HAuCl_4$ and 0.006 M $CoCl_2 \cdot 6H_2O$ or 0.006 M $NiCl_2 \cdot 6H_2O$ aqueous solutions were mixed under stirring, and the pH was adjusted to 10 by adding drops of a NaOH solution. Then, appropriate amounts of carbon black (C_{black}) and $NaBH_4$ were added to the solution under vigorous stirring. The molar ratio of metals:$NaBH_4$ was fixed to 1:3. After 4 h, the black powder was collected by centrifugation, washed several times with water:ethanol 1:1 mixture, and dried at 80°C overnight.

2.2 Preparation of carbon-supported Au:Co and Au:Ni nanoalloys by ethylene glycol-stabilization method (Au:Co/C-EG, Au:Ni/C-EG)

Au:Co/C-EG and Au:Ni/C-EG catalysts were prepared by the so-called ethylene glycol-stabilization method (EG) at room temperature. For this purpose, equal volumes of 0.001 M $HAuCl_4$/EG and 0.001 M $CoCl_2 \cdot 6H_2O$/EG or 0.001 M $NiCl_2 \cdot 6H_2O$/EG were mixed under stirring. Then, appropriate amounts of C_{black} and $NaBH_4$ were added to the solution under vigorous stirring. The molar ratio of metals:$NaBH_4$ was fixed to 1:20. After 4 h, the black powder was collected by centrifugation, washed several times with water:ethanol 1:1 mixture, and dried at 80°C overnight.

2.3 Preparation of carbon-supported Au (Au/C) by hydrothermal method

The Au/C composite was prepared to compare the electrocatalytic activity of the materials. A volume of $HAuCl_4$ aqueous solution was placed into a Teflon vessel, and the pH was adjusted to 10. Then, C_{black} and $NaBH_4$ were added. The molar ratio of Au:$NaBH_4$ was fixed to 1:3. The above solution was transferred to a Teflon lined

autoclave and heated to 180°C for 4 h. The resulting black powder was filtrated, washed repeatedly with water:ethanol 1:1 mixture, and dried at 80°C overnight.

2.4 Characterization

Crystallographic studies and phase determination were made by X-ray diffraction, DRX (Bruker 2D Phaser, Billerica, Massachusetts, USA) at room temperature, using Cu–Kα (λ = 1.5418 Å) radiation. X-ray scans were carried out from 5 ° to 90 ° in 2θ, in steps of 0.5 ° and time of 0.5 s.

The obtained carbon-supported nanoparticles shape, size, size distribution, and local chemical analysis were studied with a transmission electron microscope, TEM (JEOL 2010 TEM, 200 kV, point to point resolution 0.19 nm), coupled with an energy-dispersive X-ray spectroscopy detector, X-EDS (INCA Energy TEM 100X). For this purpose, one drop of the catalyst slurry was placed on a copper TEM grid, followed by drying at room temperature.

Inductively coupled plasma mass spectrometry, ICP-MS (NexION 2000, PerkinElmer, Waltham, MA, USA), was used to determine the catalysts composition, analyzes were made in standard mode with calibration using an internal standard (Rh-103). X-ray photoelectron spectroscopy, XPS patterns were obtained using a Thermo Scientific K-alpha spectrometer with a monochromate Al X-ray source (hν = 1486.6 eV; spot size 400 μm). Pass energies of 30 and 100 eV were used to record the core level and the survey spectra, respectively. All spectra were acquired using an electron flood gun to compensate possible positive charge accumulation during measurements. The obtained spectra were deconvoluted and fitted using Thermo Scientific Advantage Software.

2.5 Electrochemical measurements.

Electrochemical tests were carried out in a standard three-electrode cell connected to an electrochemical station (VMP2, BioLogic Science Instruments, Seyssinet-Pariset, France) with a glassy carbon plate as the counter electrode and a Hg/HgO (0.1 M KOH) as the reference electrode; all the potential values are nevertheless expressed on the reversible hydrogen electrode (RHE) scale (equation 1).

$$E_{\mathrm{RHE}} = E_{\mathrm{Hg/HgO}} + \left(E^{o}{}_{\mathrm{Hg/HgO}} - E^{0}{}_{\mathrm{RHE}}\right) = E_{\mathrm{Hg/HgO}} + 0.932 \ [=] \ \mathrm{V} \quad (1)$$

The working electrode was a glassy-carbon rotating disk electrode (GCE, diameter: 5 mm, area: 0.2 cm^2) from Pine instruments, onto which a thin-film of the desired AuM/C electrocatalyst was formed. To that goal, the as-synthesized AuCo/C-EG, AuNi/C-EG, AuCo/C-S, AuNi/C-S, and Au/C electrocatalysts were ultrasonically dispersed, along with an amount of Nafion® 117 (powder:Nafion 1:1 mass ratio), in ethanol:water (90:10 volume ratio) solution. Afterward, two drops of 5 µL were deposited onto the surface of the glassy carbon electrode. The total metal loading of each nanoalloy was fixed at 10 µg cm^{-2}.

The electrochemical behavior of the carbon-supported nanoalloys was tested by cyclic voltammetry (CV) in Ar-saturated 0.1 M KOH from 0.032 to 1.632 V *vs* RHE, at a scan rate of 50 mV s^{-1}, from which the electrochemical surface area (ECSA) of the AuM/C electrocatalysts were determined. For this purpose, the Au-oxide reduction peak coulometry is integrated, and the ECSA is calculated as follows (equation 2),

$$ECSA = \frac{Q}{(0.386)(X_{Au})} \cdot 100[=] \ m^2 g^{-1}{}_{Au} \quad (2)$$

where Q is the total charge for the reduction of Au-oxide (mC), 0.386 is a constant assuming that a monolayer of Au oxides was formed (mC cm^{-2}), X_{Au} is the mass of Au loading (µg), and 100 is a conversion factor.

The electrocatalytic performance towards ORR was measured by cyclic voltammetry in O_2-saturated 0.1 M KOH from 0.032 to 1.631 V *vs* RHE, at 5 mV s^{-1} and rotation speeds of 225, 400, 625, 900, 1225, and 1600 rpm. From this data, kinetic markers of the ORR were determined: the onset potential and the half-wave potential of ORR. The onset potential was determined as the potential measured for a faradaic current density of -0.1 mA cm^{-2} on the ORR polarization plot recorded at 1600 rpm. The half-wave potential was determined as the potential when the current is the half of the limiting current (also on the plot at 1600 rpm). To determine the intrinsic catalytic activity of materials, specific activity at 0.85 V *vs.* RHE was determined.

Finally, the electrocatalytic stability of the materials was tested. For this purpose, the electrocatalysts were subjected to an accelerated degradation test (ADT), consisting of 5,000 continuous cycles of CV between 0.5 and 1 V *vs* RHE with a scanning rate of 100 mV s^{-1} in an O_2-saturated 0.1 M KOH, at room temperature. ECSAs

and ORR LSV polarization curves at 1600 rpm of the materials before and after the potential cycling were measured to evaluate the fate of each electrocatalyst upon the AST.

3 Results and discussion

The carbon-supported AuCo and AuNi nanoalloys prepared by two different methods were firstly characterized by powder X-ray diffraction. Figure 1 shows that all the samples crystallized in a typical face-centered cubic structure. The diffraction peaks located at 38.17 °, 44.37 °, 64.55 °, 77.53 °, and 81.69 ° in 2θ are assigned to {111}, {200}, {220}, {311}, and {222} crystallographic planes of Au. The signal at 26.6 ° in 2θ corresponds to the {002} family of planes of graphite. There are no diffraction peaks different from those of Au in Figures 1b and 1d, relative to Au:Co/C-EG and Au:Ni/C-EG, respectively; so, oxidized secondary phases of the co-metals are discarded in the cases of the EG-stabilization method. The picture changes for the stirring method. For Figure 1c (Au:Co/C-S), it is possible to distinguish a diffraction signal located at 18.88 ° in 2θ, that is indexed with the {001} family of planes of $Co(OH)_2$, while Figure 1e (Au:Ni/C-S) highlights a diffraction peak at 19.3 ° in 2θ that corresponds to the {001} crystallographic planes of β-$Ni(OH)_2$. Due to the pK_s values for $Co(OH)_2$ and $Ni(OH)_2$ (14.8 and 14.7, respectively [21]), those phases are susceptible to being formed when the pH of the solution is adjusted to alkaline values, this to prevent the $NaBH_4$ from forming H_2 gas.

Making an approaching between 36° and 40° in 2θ, figure 1 show that the diffraction peak angle for the (111) family of planes of Au was slightly higher than pure gold after the alloying process (Au/C 38.18 °, Au:Co/C-EG 38.21 °, Au:Ni/C-EG 38.22 °, Au:Ni/C-S 38.23 °, and Au:Co/C-S 38.25 ° in 2θ). It can be explained because cobalt (1.72 Å) and nickel (1.62 Å) have atomic ratios smaller than gold (1.79 Å). Broader diffraction peaks are also observed for the materials, indicating that the long-range order decreased due to the presence of Co or Ni. Crystallite size was calculated by using Scherrer equation with the line broadening at half the maximum intensity of (111) family of planes, and they turned out to be: Au/C 32 nm, Au:Co/C-EG 23 nm, Au:Ni/C-EG 14 nm, Au:Co/C-S 15 nm, and Au:Ni/C-S 13 nm. The stirring method led to smaller crystallites than ethylene-glycol stabilization ones.

Figure 1 XRD patterns of (**a**) Au/C prepared via hydrothermal; (**b**) AuCo/C prepared via EG-stabilization method; (**c**) AuCo/C prepared via stirring method; (**d**) AuNi/C prepared via EG-stabilization method; and (**e**) AuNi/C prepared via stirring method.

Shape, size, particle size distribution, and atomic composition of the catalysts onto the carbon support were investigated by TEM and X-ray energy dispersive spectroscopy. The Au/C nanoparticles have a spherical shape and show some agglomerations (Figure 2a). 66% of the particles have diameters lower than 30 nm, with an average of 28 ± 20 nm. Figures 2b and 2d correspond to the TEM micrographs of AuCo/C-EG and AuNi/C-EG, respectively. They also show particles with near-spherical morphology. 66% of AuCo/C-EG nanoparticles have diameters lower than 30 nm and an average of 32 ± 21 nm. In comparison, 20% of AuNi/C-EG nanostructures are smaller than 30 nm, with an average of 44 ± 22 nm. Ethylene glycol is a polyalcohol with three hydroxyl groups that can act as stabilization agents avoiding the nanoparticle stacking [20]. Even though, the materials obtained with EG-stabilization with the present synthesis parameters have larger average sizes than for Au/C.. Finally, although TEM micrographs of AuCo/C-S and AuNi/C-S nanoparticles show a similar morphology (near-spherical particles) and some agglomerates (Figure 2c and 2e), it is noticed that 64% and 89% of the particles have significantly lower diameters: less than 15 nm, with means of 17 ± 16 nm, and 10 ± 5 nm, respectively. As seen, particle sizes determined with TEM analysis are bigger than crystallite sizes calculated from XRD measurements; this agrees with the fact that a particle is always larger and may consist of several crystals. This is particularly obvious for the bimetallic samples prepared by the EG-stabilization method.

X-EDS chemical analysis revealed that Co and Ni atomic ratios *versus* Au are 0.52 and 0.26, respectively, for the materials prepared by the stirring method. These chemical compositions are however not homogeneous for the samples, the smallest particles corresponding to Co-rich or Ni-rich phases, and the largest to Au-rich phases. The former M-rich phases are probably composed by $Co(OH)_2$ or β-$Ni(OH)_2$ phases in majority, in agreement with the XRD data presented above.

Figure 2 TEM images and particle size distribution of (**a**) Au/C, (**b**) AuCo/C-EG, (**c**) AuCo/C-S, (**d**) AuNi/C-EG, and (**e**) AuNi/C-S.

Inductively coupled plasma – mass spectrometry (ICP-MS) was carried out to quantitatively determine the global Au, Co, and Ni contents of the materials on the carbon support. These results are summarized in Table

1. The low concentration of Co in the AuCo/C-EG nanoalloy may be due to the inability to generate monoanion ethylene glycol that forms cobalt ethylene glycoxide and allows to reduce the Co(II) ions [22].

Table 1 Metal content (%wt.) determined by ICP-MS

The prepared materials' electrochemical behavior was then tested in three-electrode cell configuration. The electrochemical surface area (ECSA) was firstly determined from cyclic voltammetry in supporting electrolyte, using 0.1 M KOH electrolyte with an Ar-saturated atmosphere. For the Au/C sample (Figure 3a), the cathodic peak at 1.08 V *vs.* RHE in the backward scan is related to the gold oxide reduction. Integrating this peak area enables the gold ECSA determination (in these calculations, we considered the particles had a density close to that of pure gold, which seems reasonable admitting their Au-rich composition – Table 1). The active area of Au/C is 0.16 cm^2, corresponding to an ECSA of 8.6 $m^2 g^{-1}_{Au,}$ this value being somewhat smaller than for other works [14-16], in agreement with the large particles size and non-negligible extent of agglomeration. Figure 3b shows such gold oxide reduction peaks for AuCo/C-EG and AuCo/C-S, located at 1.07 and 1.11 V *vs* RHE, respectively. The corresponding active area of the AuCo/C-EG was calculated at 0.07 cm^2 (corresponding to an ECSA of 3.9 $m^2 g^{-1}_{Au}$) and that of AuCo/C-S was significantly higher: 0.49 cm^2 (corresponding to an ECSA of 25.4 $m^2 g^{-1}_{Au}$) due to the smaller particle size of the latter sample. Figure 3b also shows a redox peak at 1.3 V *vs* RHE, which is related to the conversion of $Co(OH)_2$ to CoOOH. Figure 3c presents similar features, where a reduction peak is observed at 1.05 and 1.07 V *vs* RHE, corresponding to the reduction of gold oxide for AuNi/C-EG and AuNi/C-S, respectively, with active areas of 0.06 and 0.29 cm^2 (corresponding to ECSAs of 3.4 and 15.7 $m^2 g^{-1}_{Au}$, respectively). Finally, in Figure 3c, it is possible to see a pair of redox peaks at 1.5 V *vs* RHE in the forward scan related to the conversion of β-$Ni(OH)_2$ to NiOOH, and its reduction at 1.4 V *vs* RHE in the reverse scan. Besides, it can be appreciated in figure 3c that current peaks of Ni3+/Ni2+ are more intense for Au:Ni/C-S than those for Au:Ni/C-EG; indeed, as seen in XRD measurements, β-Ni(OH)2 was already formed in the aqueous solution stirring prepared material.

Figure 3 Cyclic voltammetry of (**a**) Au/C, (**b**) AuCo/C prepared by EG-stabilization method (black-straight line) and stirring method (blue-dashed line); (**c**) AuNi/C prepared by EG stabilization method (black-straight line) and stirring method (blue-dashed line) at 50 mV s^{-1}

To evaluate the carbon-supported materials' electrocatalytic activity towards the ORR, hydrodynamic polarization plots were acquired in the rotating disk electrode setup. Figure 4 shows the polarization curves at

1600 rpm in alkaline media at 5 mV s^{-1} for all the tested electrocatalysts; as it can be seen, some materials show ill-defined limiting current plateau after the wave at high rotating speed. This behavior is usually related to a not wholly covered glassy carbon electrode, and since the GC catalyzes the ORR at high overpotential, this background current prevents a limit current plateau from being defined [34]. The above is probably originating from the fact that the particles of Au:Co/C-EG and Au:Ni/C-EG are larger with respect to the other materials, which may lead to "discrete active layers" at low Au loading investigated here, hence non-complete overlap between the oxygen diffusion layer areas of each particle [3-36]. The faradaic ORR initiates at around E_{onset} = 0.847 V *vs* RHE for Au/C. The onset potential (E_{onset}) and the Gibbs free energy are related. The more positive the starting potential, the more negative the Gibbs free energy [23]. Figures 4a and 4b highlights that the ORR is favored in the following descending order Au/C > AuNi/C-S > AuCo/C-S > AuNi/C-EG > AuCo/C-EG; the values of onset potentials are listed in Table 2.

The half-wave potential ($E_{1/2}$) is also a good marker of the ORR kinetic activity, its value being independent of the analyte concentration. Figure 4a indicates that the Au/C has the most positive value of $E_{1/2}$: 0.654 V *vs* RHE. The materials, in descending order of the half-wave potential, are Au/C > AuNi/C-S > AuCo/C-EG ≥ AuNi/EG > AuCo/C-S. To compare the intrinsic electrocatalytic performance of the materials, we calculated the specific activity (SA) by normalizing the kinetic current (I_k) at 0.85 V *vs* RHE to the active area. As shown in figure 4c, the AuNi/C-EG has the largest specific activity at 0.85 V *vs* RHE (-0.160 mA cm^{-2}), and the lowest value of ECSA (table 2); the above indicates that this material has the most active surface sites to carry out the electroreduction of oxygen with respect to the other electrocatalysts. The particle size plays an important role in the performance of the prepared materials. On the one hand, Au:Co/C-S and Au:Ni/C-S are the smallest particles, hence they have the most significant active area and more positive onset potential. On the other hand, Au:Co/C-EG and Au:Ni/C-EG present better charge carriers transfer due to larger particle size decreased grain frontiers, which led to a higher specific activity (at 0.85 V *vs.* RHE) and half-wave potential.

Figure 4 Comparison of ORR electrochemical activities: (a) ORR polarization curves at 1600 rpm recorded in O_2-satutared 0.1 M KOH with a sweep rate of 5 mV s^{-1} of Au/C (orange), AuCo/C-EG (green), AuNi/C-EG (blue), AuCo/C-S (roed) and AuNi/C-S (black); (b) zoom of the ORR polarization curves; (c) Specific activities at 0.85 V *vs.* RHE

Table 2 summarizes the results of electrochemical active surface area, onset potential, half-wave potential, and specific activity at 0.85 V *vs.* RHE.

Table 2 Summary of ECSA ($cm^2\ g^{-1}_{Au}$), E_{onset} (V), $E_{1/2}$ (V), and SA (mA cm^{-2}) at 0.85 V *vs.* RHE with standard deviation

The electrocatalytic stability of the materials is also an essential parameter for practical applications. Figure 5 shows the CV and ORR polarization curves before and after the ADT of AuCo/C-EG and AuNi/C-EG. As shown in Figure 5a, the current peaks related to the redox pairs of Co suffered a loss in intensity after the ADT, indicating leaching of the transition metal. In figure 5c it is possible to notice that the electrochemical profile of Au:Ni/C-EG shifted to more positive potentials, indicating a possible leaching of Ni, since if the potential at which the oxidation increases, the reaction is thermodynamically unfavored. Besides, it was observed losses of 20% and 21% in the Au active areas of AuCo/C-EG and AuNi/C-EG, respectively.

As illustrated in Figure 5b, after the 5,000 cycles of ADT, the AuCo/C-EG material does not well retain its catalytic activity: it shows 54 and 43 mV negative shifts for E_{onset} and $E_{1/2}$, respectively. On the other hand, as shown in Figure 5d, the AuNi/C-EG electrocatalyst better keeps its catalytic activity. It presented negative shifts of 16 and 32 mV for E_{onset} and $E_{1/2}$. Besides, the AuCo/C-EG lost about 80 % of its SA, meanwhile the AuNi/C-EG lost 6 % (table 3). This enhanced stability of the Ni-containing sample originates from the considerably more positive Nernst potential for Ni than for Co, making Ni more stable to corrosion [5].

Figure 5 Comparison of ORR activities of AuCo/C-EG and AuNi/C-EG before and after 5,000 CVs; (a) CV curves of AuCo/C-EG in Ar-saturated 0.1 M KOH at a sweep rate of 50 mV s^{-1}. (b) ORR polarization curves at 1600 rpm of AuCo/C-EG in O_2-saturated 0.1 M KOH. (c) CV curves of AuNi/C-EG in Ar-saturated 0.1 M KOH at a sweep rate of 50 mV s^{-1}. (d) ORR polarization curves at 1600 rpm of AuNi/C-EG in O_2 saturated 0.1 M KOH.

Table 3 summarizes the electrochemical active area, onset potential and half-wave potential after the 5,000 cycles of CV.

Table 3 Summary of Active area (cm^{-2}), E_{onset} (V), $E_{1/2}$ (V), and SA (mA cm^{-2}) at 0.85 V *vs.* RHE with standard deviation after 5,000 cycles of ADT

Figure 6 shows the 4f core-level (CL) spectra of Au/C, AuNi/C-EG initial, and AuNi/C-EG after 5,000 cycles of ADT. The binding energies of all spectra were fixed in reference to C 1s binding energy of 285 eV. Au/C displays a doublet at binding energies of 88.1 and 84.5 eV, which are assigned to Au $4f_{5/2}$ and Au $4f_{7/2}$, respectively, and both corresponds to zero-valent Au^0 [24-25]. After the alloying with Ni, the AuNi/C-EG CL spectrum shows two sharp peaks located at binding energies of 88.0 and 84.3 eV related to Au $4f_{5/2}$ and Au $4f_{7/2}$, respectively. This negative shift in the binding energy proves that the AuNi/C-EG exists in nanoalloy form

[26]. More critical, previous works showed that these shifts in the binding energy indicate a change in the d-band structure of Au [27-28]. When the CL shifts to lower values, the d-band center presents a positive shift of the Fermi level, which will result in a better adsorption of oxygen-containing species onto the gold surface and better electrocatalytic activity towards the ORR [29-30], being admitted that pure Au does not bind oxygen enough strongly to be really ORR active. After the 5,000 cycles of ADT, the CL of AuNi/C-EG shifted to more positive values than those for AuNi/C-EG, explaining the decrease in the electrocatalytic activity.

Figure 6 XPS Au 4f fitted-spectra of Au/C, AuNi/C-EG initial, and AuNi/C-EG after 5,000 cycles of ADT

Conclusions

In this work, and for the first time, carbon-supported bimetallic AuCo and AuNi electrocatalysts were prepared by ethylene glycol-stabilization and aqueous-solution stirring, and evaluated for the oxygen reduction reaction (ORR) in alkaline media. All the materials exhibit near-spherical nanoparticles of rather large sizes. The stirring method produced smaller and less agglomerated particles than the ethylene glycol method. The XPS analysis of AuNi/C-EG showed that Ni atoms can affect the electronic structure of Au, since the Au $4f_{5/2}$ and Au $4f_{7/2}$ core levels showed changes in binding energies of –0.1 and –0.2 eV, respectively, resulting in an upshift in the d-band structure of Au for the nanoalloys. This proves that small amounts of Co or Ni were incorporated into the Au lattice. This led to increased electrocatalytic activity towards the oxygen reduction reaction in alkaline media, as expressed in terms of specific activity. The durability of the nanoalloys was also found superior to that of Au/C, although in slight amount. The results obtained in this work evidence that Au-based nanoalloys, prepared ethylene glycol stabilization, and aqueous solution stirring have potential application as electrocatalysts for the oxygen reduction reaction in alkaline electrolyte. It opens the possibility of modifying characteristics such as composition, size, and particle distribution, thus improving the electrocatalytic activity of materials, taking advantage of the benefits of mild chemistry methods.

Acknowledgments

This research was supported by the SEP-CONACyT 236812 project. The authors acknowledge the Mexican National Council of Science and Technology for the PhD research scholarship of F. Acosta (CVU 781349).

References

[1] Hren, M., Božič, M., Fakin, D., Kleinschek, K. S., & Gorgieva, S. (2020). Alkaline membrane fuel cells: anion exchange membranes and fuels. *Sustainable Energy & Fuels*.

[2] Shao, M., Chang, Q., Dodelet, J. P., & Chenitz, R. (2016). Recent advances in electrocatalysts for oxygen reduction reaction. *Chemical reviews*, *116*(6), 3594-3657.

[3] Vinayan, B. P., & Ramaprabhu, S. (2013). Platinum–TM (TM= Fe, Co) alloy nanoparticles dispersed nitrogen doped (reduced graphene oxide-multiwalled carbon nanotube) hybrid structure cathode electrocatalysts for high performance PEMFC applications. *Nanoscale*, *5*(11), 5109-5118.

[4] Liu, T., Wang, K., Yuan, Q., Shen, Z., Wang, Y., Zhang, Q., & Wang, X. (2017). Monodispersed sub-5.0 nm PtCu nanoalloys as enhanced bifunctional electrocatalysts for oxygen reduction reaction and ethanol oxidation reaction. *Nanoscale*, *9*(9), 2963-2968.

[5] Han, B., Carlton, C. E., Suntivich, J., Xu, Z., & Shao-Horn, Y. (2015). Oxygen reduction activity and stability trends of bimetallic $Pt_{0.5}M_{0.5}$ nanoparticle in acid. *The Journal of Physical Chemistry C*, *119*(8), 3971-3978.

[6] Zadick, A., Dubau, L., Sergent, N., Berthome, G., & Chatenet, M. (2015). Huge instability of Pt/C catalysts in alkaline medium. *Acs Catalysis*, *5*(8), 4819-4824.

[7] Zhang, J., Sasaki, K., Sutter, E., & Adzic, R. R. (2007). Stabilization of platinum oxygen-reduction electrocatalysts using gold clusters. *Science*, *315*(5809), 220-222.

[8] Park, H. Y., Jeon, T. Y., Jang, J. H., Yoo, S. J., Choi, K. H., Jung, N., ... & Sung, Y. E. (2013). Enhancement of oxygen reduction reaction on PtAu nanoparticles via CO induced surface Pt enrichment. *Applied Catalysis B: Environmental*, *129*, 375-381.

[9] Cherevko, S., Zeradjanin, A. R., Keeley, G. P., & Mayrhofer, K. J. (2014). A comparative study on gold and platinum dissolution in acidic and alkaline media. *Journal of The Electrochemical Society*, *161*(12), H822.

[10] Nørskov, J. K., Rossmeisl, J., Logadottir, A., Lindqvist, L. R. K. J., Kitchin, J. R., Bligaard, T., & Jonsson, H. (2004). Origin of the overpotential for oxygen reduction at a fuel-cell cathode. *The Journal of Physical Chemistry B*, *108*(46), 17886-17892.

[11] Kusada, K., Wu, D., Yamamoto, T., Toriyama, T., Matsumura, S., Xie, W., ... & Kitagawa, H. (2019). Emergence of high ORR activity through controlling local density-of-states by alloying immiscible Au and Ir. *Chemical science*, *10*(3), 652-656.

[12] Negro, E., Delpeuch, A. B., Vezzù, K., Polizzi, S., Bertasi, F., Nawn, G., ... & Di Noto, V. (2016). Graphene-Supported Au-Ni Carbon Nitride Electrocatalysts for the ORR in Alkaline Environment. *ECS Transactions*, *72*(29), 1.

[13] Gong, H., Lu, S., Strasser, P., & Yang, R. (2018). Highly efficient AuNi-Cu_2O electrocatalysts for the oxygen reduction and evolution reactions: Important role of interaction between Au and Ni engineered by leaching of Cu_2O. *Electrochimica Acta*, *283*, 1411-1417.

[14] Wang, J., Chen, F., Jin, Y., & Johnston, R. L. (2016). Highly active and stable AuNi dendrites as an electrocatalyst for the oxygen reduction reaction in alkaline media. *Journal of Materials Chemistry A*, *4*(45), 17828-17837.

[15] Wang, J., Chen, F., Jin, Y., Lei, Y., & Johnston, R. L. (2017). One-Pot Synthesis of Dealloyed AuNi Nanodendrite as a Bifunctional Electrocatalyst for Oxygen Reduction and Borohydride Oxidation Reaction. *Advanced Functional Materials*, *27*(23), 1700260.

[16] Wang, J., Chen, F., Jin, Y., & Johnston, R. L. (2018). Gold–Copper Aerogels with Intriguing Surface Electronic Modulation as Highly Active and Stable Electrocatalysts for Oxygen Reduction and Borohydride Oxidation. *ChemSusChem*, *11*(8), 1354-1364.

[17] Ly, A., Asset, T., & Atanassov, P. (2020). Integrating nanostructured Pt-based electrocatalysts in proton exchange membrane fuel cells. *Journal of Power Sources*, *478*, 228516.

[18] Zhou, Z., Wang, S., Zhou, W., Wang, G., Jiang, L., Li, W., ... & Xin, Q. (2003). Novel synthesis of highly active Pt/C cathode electrocatalyst for direct methanol fuel cell. *Chemical communications*, (3), 394-395.

[19] Li, W., Liang, C., Zhou, W., Qiu, J., Zhou, Z., Sun, G., & Xin, Q. (2003). Preparation and characterization of multiwalled carbon nanotube-supported platinum for cathode catalysts of direct methanol fuel cells. *The Journal of Physical Chemistry B*, *107*(26), 6292-6299.

[20] Yan, Z., Wang, M., Liu, J., Liu, R., & Zhao, J. (2014). Glycerol-stabilized $NaBH_4$ reduction at room-temperature for the synthesis of a carbon-supported PtxFe alloy with superior oxygen reduction activity for a microbial fuel cell. *Electrochimica Acta*, *141*, 331-339.

[21] Blais, J. F., Djedidi, Z., Cheikh, R. B., Tyagi, R. D., & Mercier, G. (2008). Metals precipitation from effluents. *Practice Periodical of Hazardous, Toxic, and Radioactive Waste Management*, *12*(3), 135-149.

[22] Matsumoto, T., Takahashi, K., Kitagishi, K., Shinoda, K., Huaman, J. L. C., Piquemal, J. Y., & Jeyadevan, B. (2015). Dissolution and reduction of cobalt ions in the polyol process using ethylene glycol: Identification of the active species and its role. *New Journal of Chemistry*, *39*(6), 5008-5018.

[23] Wang, Y., & Balbuena, P. B. (2005). Design of oxygen reduction bimetallic catalysts: ab-initio-derived thermodynamic guidelines. *The Journal of Physical Chemistry B*, *109*(40), 18902-18906.

[24] Naveen, M. H., Gurudatt, N. G., Noh, H. B., & Shim, Y. B. (2016). Dealloyed AuNi dendrite anchored on a functionalized conducting polymer for improved catalytic oxygen reduction and hydrogen peroxide sensing in living cells. *Advanced Functional Materials*, *26*(10), 1590-1601.

[25] Li, X. R., Li, X. L., Xu, M. C., Xu, J. J., & Chen, H. Y. (2014). Gold nanodendrities on graphene oxide nanosheets for oxygen reduction reaction. *Journal of Materials Chemistry A*, *2*(6), 1697-1703.

[26] Duan, H., & Xu, C. (2016). Nanoporous PdCr alloys as highly active electrocatalysts for oxygen reduction reaction. *Physical Chemistry Chemical Physics*, *18*(5), 4166-4173.

[27] Wang, G., Xiao, L., Huang, B., Ren, Z., Tang, X., Zhuang, L., & Lu, J. (2012). AuCu intermetallic nanoparticles: surfactant-free synthesis and novel electrochemistry. *Journal of Materials Chemistry*, *22*(31), 15769-15774.

[28] Yang, T., de Almeida, C. M. R., Ramasamy, D., & Loureiro, F. J. A. (2014). A detailed study of Au–Ni bimetal synthesized by the phase separation mechanism for the cathode of low-temperature solid oxide fuel cells. *Journal of Power Sources*, *269*, 46-53.

[29] Lima, F. H. B., Zhang, J., Shao, M. H., Sasaki, K., Vukmirovic, M. B., Ticianelli, A. E., & Adzic, R. R. (2007). Catalytic activity− d-band center correlation for the O_2 reduction reaction on platinum in alkaline solutions. *The Journal of Physical Chemistry C*, *111*(1), 404-410.

[30] Wu, X., Chen, F., Zhang, N., Lei, Y., Jin, Y., Qaseem, A., & Johnston, R. L. (2017). Activity trends of binary silver alloy nanocatalysts for oxygen reduction reaction in alkaline media. *Small*, *13*(15), 1603387.

[31] Promanan, T., & Sarakonsri, T. (2017). SYNTHESIS AND CHARACTERIZATION OF PALLADIUM-BASED NANO-CATALYST ON N-DOPED GRAPHENE FOR DIRECT ETHANOL FUEL CELLS. *Reviews on Advanced Materials Science*, *52*.

[32] Sudirman, S., Adi, W. A., Budianto, E., & Yudianti, R. (2020). Mono-Dispersed Pt/MWNTs: Growing Directly on Multiwall Carbon Nanotubes (MWNTs) Using NaBH4 as Reducing Agent for Component of Proton Exchange Membrane Fuel Cell (PEMFC). *International Journal of Chemistry*, *12*(1), 37-48.

[33] Ulas, B., Caglar, A., Kivrak, A., & Kivrak, H. (2019). Atomic molar ratio optimization of carbon nanotube supported PdAuCo catalysts for ethylene glycol and methanol electrooxidation in alkaline media. *Chemical Papers*, *73*(2), 425-434.

[34] Khadke, P., Tichter, T., Boettcher, T., Muench, F., Ensinger, W., & Roth, C. (2021). A simple and effective method for the accurate extraction of kinetic parameters using differential Tafel plots. *Scientific reports*, *11*(1), 1-15.

[35] Nesselberger, M., Roefzaad, M., Hamou, R. F., Biedermann, P. U., Schweinberger, F. F., Kunz, S., ... & Arenz, M. (2013). The effect of particle proximity on the oxygen reduction rate of size-selected platinum clusters. *Nature materials*, *12*(10), 919-924.

[36] Inaba, M., Zana, A., Quinson, J., Bizzotto, F., Dosche, C., Dworzak, A., ... & Arenz, M. (2021). The Oxygen Reduction Reaction on Pt: Why Particle Size and Interparticle Distance Matter. *ACS Catalysis*, *11*, 7144-7153.

Figure 1

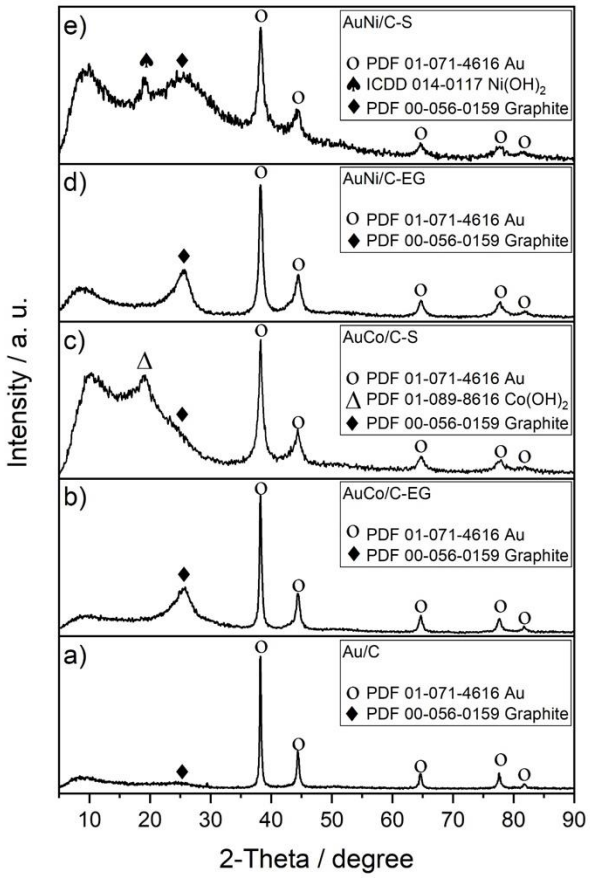

Figure 1 XRD patterns of (**a**) Au/C prepared via hydrothermal; (**b**) AuCo/C prepared via EG-stabilization method; (**c**) AuCo/C prepared via stirring method; (**d**) AuNi/C prepared via EG-stabilization method; and (**e**) AuNi/C prepared via stirring method.

Figure 2

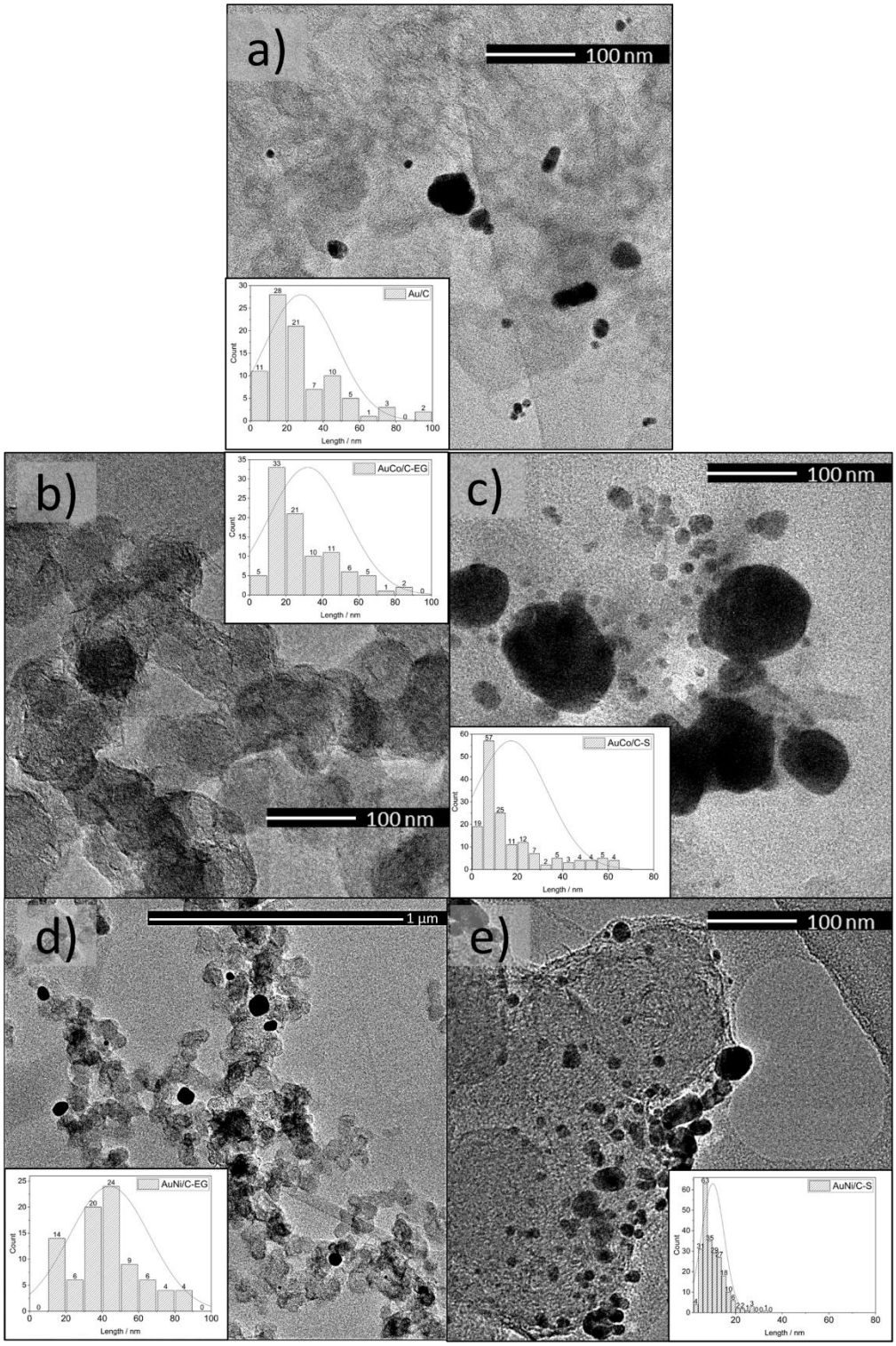

Figure 2 TEM images and particle size distribution of (**a**) Au/C, (**b**) AuCo/C-EG, (**c**) AuCo/C-S, (**d**) AuNi/C-EG, and (**e**) AuNi/C-S.

Figure 3

Figure 3 Cyclic voltammetry of (**a**) Au/C, (**b**) AuCo/C prepared by EG-stabilization method (black-straight line) and stirring method (blue-dashed line); (**c**) AuNi/C prepared by EG stabilization method (black-straight line) and stirring method (blue-dashed line) at 50 mV s^{-1}

Figure 4

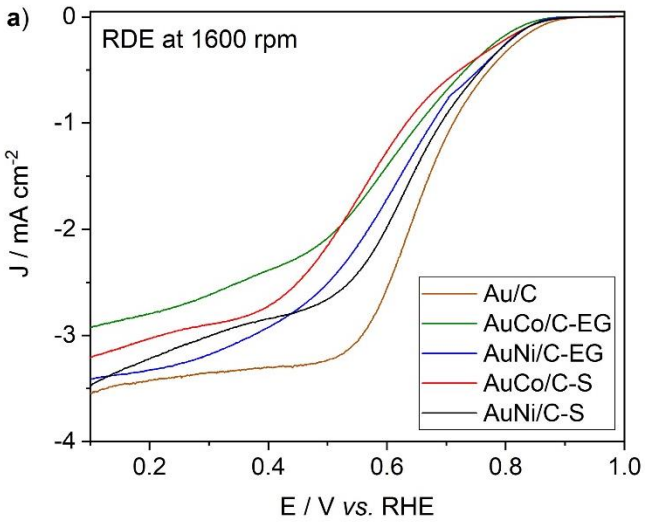

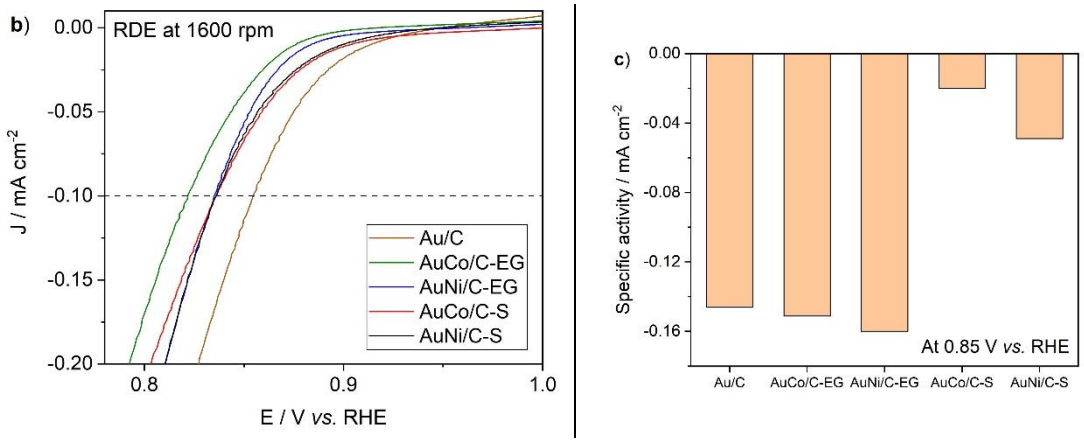

Figure 4 Comparison of ORR electrochemical activities: (a) ORR polarization curves at 1600 rpm recorded in O_2-satutared 0.1 M KOH with a sweep rate of 5 mV s^{-1} of Au/C (orange), AuCo/C-EG (green), AuNi/C-EG (blue), AuCo/C-S (red) and AuNi/C-S (black); (b) zoom of the ORR polarization curves; (c) Specific activities at 0.85 V *vs.* RHE

Figure 5

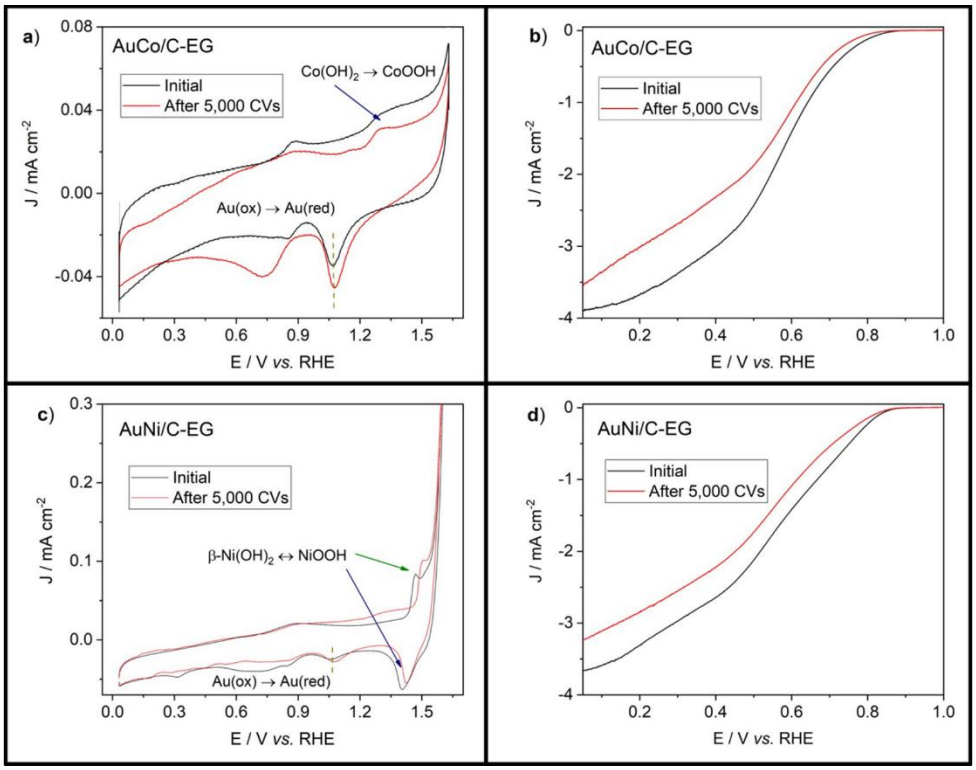

Figure 5 Comparison of ORR activities of AuCo/C-EG and AuNi/C-EG before and after 5,000 CVs; (a) CV curves of AuCo/C-EG in Ar-saturated 0.1 M KOH at a sweep rate of 50 mV s^{-1}. (b) ORR polarization curves at 1600 rpm of AuCo/C-EG in O_2-saturated 0.1 M KOH. (c) CV curves of AuNi/C-EG in Ar-saturated 0.1 M KOH at a sweep rate of 50 mV s^{-1}. (d) ORR polarization curves at 1600 rpm of AuNi/C-EG in O_2 saturated 0.1 M KOH.

Figure 6

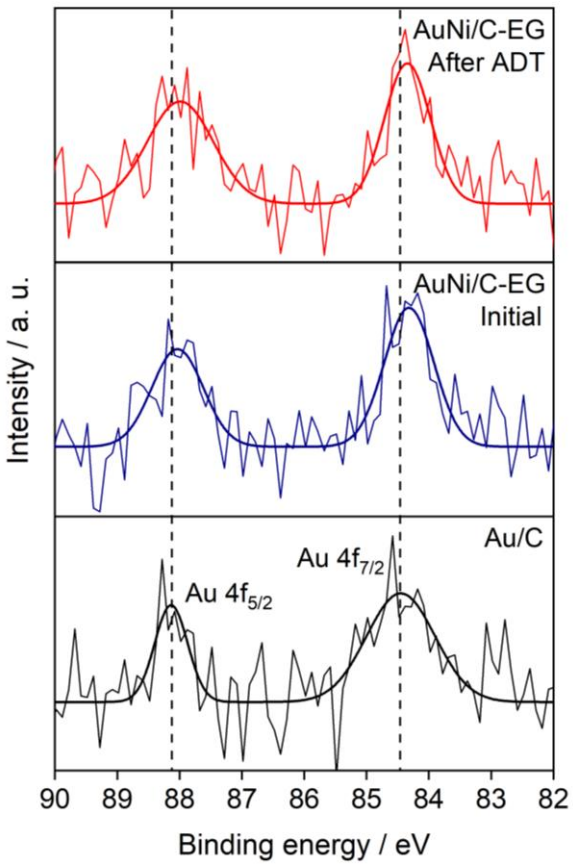

Fig. 6 XPS Au 4f fitted-spectra of Au/C, AuNi/C-EG initial, and AuNi/C-EG after 5,000 cycles of ADT

Table 1

Table 1 Metal content determined by ICP-MS

	Atomic percent (%)			Weight percent (%)		
Material	Au	Co	Ni	Au	Co	Ni
Au/C	99	-	-	19	-	-
AuCo/C EG	99	0.002	-	9.2	0.02	-
AuNi/C EG	94	-	6	9.6	-	0.2

*For the atomic percentage, only the proportion of metals was considered. In the percentage by weight, the carbon support was also considered.

Table 2

Table 2 Summary of ECSA ($cm^2\ g^{-1}_{Au}$), E_{onset} (V), $E_{1/2}$ (V), and SA ($mA\ cm^{-2}$) at 0.85 V *vs.* RHE with standard deviation

Electrocatalyst	ECSA / $cm^2\ g^{-1}_{Au}$ ± SD	E_{onset} / V *vs.* RHE ± SD	$E_{1/2}$ / V *vs.* RHE ± SD	SA / $mA\ cm^{-2}$ ± SD at 0.85 V *vs.* RHE
Au/C	8.6 ± 0.6	0.847 ± 0.012	0.654 ± 0.009	-0.146 ± 0.002
AuCo/C-EG	3.9 ± 0.3	0.827 ± 0.006	0.612 ± 0.006	-0.151 ± 0.002
AuNi/C-EG	3.4 ± 0.3	0.833 ± 0.004	0.606 ± 0.006	-0.160 ± 0.007
AuCo/C-S	25.4 ± 1.4	0.835 ± 0.009	0.580 ± 0.006	-0.020 ± 0.003
AuNi/C-S	15.7 ± 0.6	0.839 ± 0.004	0.643 ± 0.001	-0.049 ± 0.002

Table 3

Table 3 Summary of Active area (cm^{-2}), E_{onset} (V), $E_{1/2}$ (V), and SA ($mA\ cm^{-2}$) at 0.85 V *vs.* RHE with standard deviation after 5,000 cycles of ADT

Electrocatalyst	Active area / cm^{-2} ± SD	E_{onset} / V *vs.* RHE ± SD	$E_{1/2}$ / V *vs.* RHE ± SD	SA / $mA\ cm^{-2}$ ± SD at 0.85 V *vs.* RHE
AuCo/C-EG	0.059 ± 0.002	0.773 ± 0.004	0.569 ± 0.003	-0.029 ± 0.002
AuNi/C-EG	0.045 ± 0.002	0.817 ± 0.002	0.574 ± 0.003	-0.150 ± 0.005

1
2
3
4
5
6
7
8
9
10
11
12
13
14
15
16
17
18
19
20
21